Journal Pre-proof

Characterization of structure, chemical bond and microwave dielectric properties in $Ca_{0.61}Nd_{0.26}TiO_3$ ceramic substituted by chromium for titanium

Zhe Xiong, Bin Tang, Fuchuan Luo, Hongyu Yang, Xing Zhang, Chengtao Yang, Zixuan Fang, Shuren Zhang

PII: S0925-8388(20)31612-1

DOI: https://doi.org/10.1016/j.jallcom.2020.155249

Reference: JALCOM 155249

To appear in: *Journal of Alloys and Compounds*

Received Date: 13 January 2020

Revised Date: 26 March 2020

Accepted Date: 16 April 2020

Please cite this article as: Z. Xiong, B. Tang, F. Luo, H. Yang, X. Zhang, C. Yang, Z. Fang, S. Zhang, Characterization of structure, chemical bond and microwave dielectric properties in $Ca_{0.61}Nd_{0.26}TiO_3$ ceramic substituted by chromium for titanium, *Journal of Alloys and Compounds* (2020), doi: https://doi.org/10.1016/j.jallcom.2020.155249.

Zhe Xiong: Conceptualization, Validation, Formal analysis, Investigation, Writing - Original Draft
Bin Tang: Resources, Validation, Funding acquisition
Fuchuan Luo: Investigation, Writing - Original Draft
Hongyu Yang: Data Curation, Writing - Review & Editing
Xing Zhang: Data Curation, Writing - Review & Editing
Chengtao Yang: Resources, Project administration
Zixuan Fang: Writing - Review & Editing
Shuren Zhang: Supervision

Characterization of Structure, Chemical Bond and Microwave Dielectric Properties in $Ca_{0.61}Nd_{0.26}TiO_3$ Ceramic Substituted by Chromium for Titanium

Zhe Xiong[a,b,c], Bin Tang[a,b,*], Fuchuan Luo[a,b,d], Hongyu Yang[a,b], Xing Zhang[a,b], Chengtao Yang[a,b,*], Zixuan Fang[a,b,*], Shuren Zhang[a,b]

[a] National Engineering Research Center of Electromagnetic Radiation Control Materials, University of Electronic Science and Technology of China, Chengdu 611731, Sichuan, China.

[b] State Key Laboratory of Electronic Thin Films and Integrated Devices, University of Electronic Science and Technology of China, Chengdu 611731, Sichuan, China.

[c] Department of Nuclear Engineering, University of California at Berkeley, Berkeley, California 94720-1730, USA.

[d] Department of Materials Science and Engineering, University of California at Berkeley, Berkeley, California 94720-1730, USA.

Bin Tang[*]: tangbin@uestc.edu.cn

Chengtao Yang[*]: ctyang@uestc.edu.cn

Zixuan Fang[*]: zixuanfang@uestc.edu.cn

ABSTRACT:

We studied the phase constitutions, microstructure, chemical bond and microwave dielectric properties for $Ca_{0.61}Nd_{0.26}Ti_{1-x}Cr_xO_3$ ($0 \le x \le 0.03$) ceramics synthesized by solid-state reaction using SEM, X-ray diffractometer, Raman spectroscopy, microwave measuring system, etc. Although the second phase TiO_2 appeared when $x \ge 0.015$ as presented in XRD patterns, TiO_2 was confirmed to have no effects on the tendency of microwave dielectric properties as a function of x value. The SEM images showed that the grain size decreased as Cr content increased, which could be explained by that doping Cr increased the grain boundary energy or decreased surface energy for $Ca_{0.61}Nd_{0.26}TiO_3$ ceramic. The SRO effects enhanced with increase of Cr substitution, which was verified by Raman spectra. The dielectric constant and τ_f value were concerned with the average ionicity of chemical bond and the ionic polarizability for $Ca_{0.61}Nd_{0.26}Ti_{1-x}Cr_xO_3$ ceramics. The SEM images suggested that the optimized sintering temperatures was 1400 ºC for samples with x =0.01. The XPS spectra and the trend of Q×f value indicated that the

balanced amount of Cr substitution could restrain the generation of Ti^{3+}. Hence, the Q×f value of $Ca_{0.61}Nd_{0.26}Ti_{1-x}Cr_xO_3$ ceramics reached the maximum of 16,078 GHz at x = 0.01 compared with that of 11,425 GHz in pure $Ca_{0.61}Nd_{0.26}TiO_3$ ceramic.

Keywords: Microwave dielectric ceramics, Chemical bond, Oxygen deficiency, Suppression of Ti^{3+}

1. Introduction

The communication technology and related hardware installations have promoted tremendous development of microwave dielectric ceramics, widely used as dielectric antennas, dielectric substrate, and dielectric resonators, etc[1-4]. The studies of antenna substrate made of ceramics and low temperature co-fired ceramic technology (LTCC) or ultra-low temperature co-fired ceramic technology (ULTCC) have captured a lot of attention for the past few years[5-7]. Furthermore, for dielectric resonators, the ceramics must present a relative high dielectric constant (ε_r) to meet the demand of devices miniaturization (size of a dielectric resonator ~ $\varepsilon_r^{-1/2}$). Also high quality factor (Q×f) and nearly zero temperature coefficient of resonant frequency (τ_f) are vital for high frequency selectivity and stability, respectively[8].

The dielectric resonators made of $CaTiO_3$-based ceramics are extensively used in civilian mobile communication system because of its high dielectric constant of 180[3, 9-14], and many literatures have concentrated on tuning its microwave dielectric properties to satisfy actual application preferably. Considering the highly positive τ_f value of +800 ppm/ºC and low Q×f value of 6,000 GHz for pure $CaTiO_3$ ceramic[10], many efforts are taken to combine it with opposite τ_f value ceramics, such as $MgTiO_3$[15], $Sm(Co_{1/2}Ti_{1/2})O_3$[16], $Re(Co_{1/2}Ti_{1/2})O_3$ (Re=La and Nd)[17], $LnMO_3$ (Ln–La, Nd; M–Al, Ga)[18], $Mg_4Nb_2O_9$[19], K_2MoO_4[20], etc. Although high Q×f value and near zero τ_f value could be obtained in this way, the dielectric constant of synthetic ceramics has been reduced to 60. Many studies have confirmed that lanthanide (trivalent ions as La^{3+}, Sm^{3+} and Nd^{3+}) ion has some positive effects to improvements of Q×f and τ_f values and keep high dielectric constant (≥ 100)

in $CaTiO_3$ ceramic[11, 14, 21]. In this $Ca_{1-x}Ln_{2x/3}TiO_3$ (Ln = Nd, Sm, La) system, $Ca_{0.61}Nd_{0.26}TiO_3$ exhibits excellent microwave dielectric properties of $\varepsilon_r \sim 108$, Q×f ~ 17,200 GHz, and $\tau_f \sim +270$ ppm/ºC[11]. As shown in Figure 1, trivalent ion Nd^{3+} substitutes for divalent ion Ca^{2+} at A-site where vacancy is introduced simultaneously to conserve charge neutrality in orthorhombic perovskite-structured $Ca_{0.61}Nd_{0.26}TiO_3$ crystal. The orthorhombic perovskite structure presents a most common distortion: the tilt of octahedrons, with respect to the ideal cubic perovskite.

As noted above, most of these studies have only concentrated on tuning the τ_f value of the $Ca_{0.61}Nd_{0.26}TiO_3$ ceramic to near zero by substitution of A or B site in perovskite structure or combining other ceramics with opposite τ_f value. Nevertheless, many researchers failed to obtain the pure $Ca_{0.61}Nd_{0.26}TiO_3$ ceramic with high Q×f value of 17,200 GHz sintering $Ca_{0.61}Nd_{0.26}TiO_3$ ceramic in air[10, 11, 22-24]. In these works, the pure $Ca_{0.61}Nd_{0.26}TiO_3$ ceramics have a low Q×f value under 17,200 GHz, which is interpreted as a result of oxygen deficiency[25, 26]. When the $Ca_{0.61}Nd_{0.26}TiO_3$ ceramic is sintered at temperature of 1350 ºC to 1450 ºC in an airtight sintering furnace, lower oxygen partial pressure leads to more Ti^{3+} ions, as described by reactions (1)-(2).

$$O_O^{\times} \leftrightarrow V_O^{\cdot\cdot} + 2e' + \frac{1}{2}O_2 \uparrow \quad (1)$$

$$Ti_{Ti}^{\times} + e' \leftrightarrow Ti_i^{\cdots} \quad (2)$$

Analogously, this phenomenon also exists in other ceramics, such as TiO_2[26], $BaZn_2Ti_4O_{11}$[27], $Ba_{4.2}Sm_{9.2}Ti_{18}O_{54}$[28], $Ba_{4.2}Nd_{9.2}Ti_{18}O_{54}$[29], $Ba_{3.75}Nd_{9.5}Ti_{18}O_{54}$[30, 31], $Na_{0.5}Sm_{0.5}TiO_3$[32], and so on. Aiming at solving this problem, Lowndes et al.[33] added moderate amounts of Mn_2O_3 in $Ca_{0.61}Nd_{0.26}TiO_3$ ceramic to refrain the generation of oxygen deficiency. Templeton et al.[25] determined that acceptor doping TiO_2 with stable divalent and trivalent cations, such as Mg, Cu, Cr and Al was an appropriate method to prevent Ti^{4+} reduction. Hence, $Ca_{0.61}Nd_{0.26}Ti_{1-x}Cr_xO_3$ ($0 \le x \le 0.03$) ceramics were proposed in this work for the purpose of Q×f value

improvement. In addition, the dependence between structure, chemical bond and microwave dielectric properties was investigated by P-V-L theory[34].

2. Experimental section

The mixed raw powder of $Ca_{0.61}Nd_{0.26}Ti_{1-x}Cr_xO_3$ ($0 \leq x \leq 0.03$) ceramics was synthesized by solid-state reaction method. Crude materials ($CaCO_3$ (≥99.5%), Nd_2O_3 (≥99.9%), TiO_2 (>99.5%) and Cr_2O_3 (≥99.9%)) were weighted proportionately in accordance with a molar ratio 0.61:0.13:1-*x*:0.5*x*. Then these raw powders in the stoichiometric ratio were milled for 6 h at the speed of 280 rpm with the ZrO_2 ball to powder weight ratio of 5:1 by planetary mill (Nanjing Machine Factory, China), followed by calcining at 1100 ℃ for 5 h. The heating rate of calcining procedure was 3℃/min. The calcined powders were re-milled with the same parameters. Then the calcined mixtures were uniaxially pressed into pellets directly with dimension of 15mm in diameter and 7mm in thickness using 5 wt.% PVA solution as binder. The samples were sintered at 1350 ℃ ~ 1450 ℃ for 4 h to obtain the dense ceramics after burning out the binder PVA at 600 ℃. The heating rate was set to 5 ℃ /min.

The microstructure and the phase components were characterized by Field Emission Scanning Electron Microscope (SEM, Electron Optics B.V, FEI, USA) and X-ray Diffractometer (XRD, X'pert Pro MPD, Philips), respectively. Rietveld refinement was employed to further understand the evolution of crystal structure using EXPGUI program. Room temperature Raman spectra was performed using a Raman microscope (LabRAM HR Evolution). The bulk density of $Ca_{0.61}Nd_{0.26}Ti_{1-x}Cr_xO_3$ ($0 \leq x \leq 0.03$) samples were measured by Archimedes method. XPS analyses were performed using an X-ray photoelectron spectrometer (XPS, Thermo scientific ESCALAB 250Xi). The dielectric constant (ε_r) and quality factor (Q×f) at microwave frequency were measured by the Hakki-Coleman method with a network analyzer (N5230A, Angilent, USA). The τ_f values were measured from difference between the resonant frequency at 25 ℃ and 85 ℃.

3. Results and discussion

3.1 Phase constitutions and microstructure analysis

Figure 2(a) shows the powder X-ray diffraction patterns of $Ca_{0.61}Nd_{0.26}Ti_{1-x}Cr_xO_3$ ($0 \le x \le 0.03$) ceramics sintered at 1400 ºC. For all investigated samples, the diffraction peaks were mainly indexed on the basis of orthorhombic perovskite-structured phase (ICSD #84348, Pnma, No. 62 space group), while small amounts of TiO_2 were detected in the range of $x \ge 0.015$. As shown in inserted left illustration of Figure 2(a), the peaks humping at $2\theta \approx 27.5^o$ was confirmed as the strongest diffraction peak of TiO_2 phase, which indicated that solid solubility of Cr^{3+} in $Ca_{0.61}Nd_{0.26}TiO_3$ ceramic is less than 0.015. Actually, the solid solubility of Cr ion presents differences among different ceramics. Tang et al[35, 36]. reported that the solid solubility of Cr in $Ba_{3.75}Nd_{9.5}Ti_{18}O_{54}$ and $CaMgSi_2O_6$ ceramics was less than 1/9 and 0.16/3, respectively. Fang et al[32] proposed that all $Na_{0.5}Sm_{0.5}TiO_3$ + x mol Cr_2O_3 ($0 \le x \le 0.015$) ceramic samples could form pure phase with orthorhombic perovskite structure. Cr additive could lead to the formation of a second phase in $MgTiO_3$ ceramic when Cr is at high doping levels[37]. Moreover, the non-equivalent substitution at B-site was considered a factor of second phase formation. It has been reported that the compound ion $(Cr_{0.5}Nb_{0.5})^{4+}$ exhibited highly improved effects on properties of $Ba_{3.75}Nd_{9.5}Ti_{18}O_{54}$ ceramic, and the all investigated samples was crystallized pure phase[38]. It's worth noting that the peak for (121) lattice planes shifts to lower angle with increase of Cr additive as shown in right side illustration in the Figure 2(a). This result can be explained by Bragg law, which was discussed in the 3.2 section.

The superlattice-reflections of $Ca_{1-x}Nd_{2x/3}TiO_3$ system were considered to indicate the tilted oxygen octahedrons around Ti^{4+}, which was reported by Fu et.al[39]. According to Fu's study, the (1 3 1), (1 1 3) and (1 0 3) reflections, as shown in Figure 2(b), indicated an a− tilting and a−b+ tilting. This result of tilting mechanism is consistent with the orthorhombic a−a−b+ tilt system based on the Glazer's notation[40].

Figure 3 presents the SEM images of $Ca_{0.61}Nd_{0.26}Ti_{1-x}Cr_xO_3$ ($0 \le x \le 0.03$) ceramics sintered at 1400 ºC. All samples exhibited closely-packed grains with few pores as seen. Obviously, the large grains of about dozens of

micrometers were observed in a whole range of compositions, while a growing number of small grains were distributed and dominated in surfaces of samples as $0.02 \leq x \leq 0.03$. Also the distributions of grain size (carried out using Nano measurer software) for $Ca_{0.61}Nd_{0.26}Ti_{1-x}Cr_xO_3$ ($0 \leq x \leq 0.03$) ceramics sintered at 1400 ºC are given in Figure 4, and the AGS indicates average grain size. As x value increased to 0.025, the average grain size reduced the minimum value, which suggested that Cr ion could inhibit the grain growth of $Ca_{0.61}Nd_{0.26}TiO_3$ ceramic. This phenomenon has been observed and confirmed in other perovskite-structured ceramics doped ions such as $Pb(Zr,Ti)O_3$[41] and $Pb(Zn_{1/3}Nb_{2/3})_{0.2}(Zr_{0.5}Ti_{0.5})_{0.8}O_3$[42]. As reported by Hng[43], there was lower wettability of the liquid phase during sintering for the Cr-containing ZnO–V_2O_5 systems specimens. Therefore, we speculated that Cr increased the grain boundary energy or decreased surface energy for $Ca_{0.61}Nd_{0.26}TiO_3$ ceramic, then the grain growth was suppressed. Clearly, the average grain size increased and a few pores appeared at x = 0.03. According to the sintering theory of ceramics, the vacancy, as a point defect, played a significant role in mass transfer processes during sintering. It can be seen from the reaction (19) (as shown in section 3.4) that Cr substitution introduced the oxygen vacancy, which was conducive to the grain growth. Moreover, given the increase of the grain boundary energy or decrease of the surface energy, the average grain size increased and a few pores appeared when x = 0.03.

3.2 Rietveld refinement and chemical bond characteristics

The Rietveld refinement was carried out using GSAS program to investigate the effects of the substitution of Cr for Ti on the structure and bond for $Ca_{0.61}Nd_{0.26}TiO_3$ ceramic. The refined XRD patterns are plotted in Figure 5 and the results of refined crystallographic data are listed in Table 1. As shown in Figure 5, the black fork and red line are experimental data and calculated profile, and the green line represents the difference between them. The blue and magenta vertical bars indicate Bragg positions of $Ca_{0.61}Nd_{0.26}TiO_3$ and TiO_2, respectively. The smoothness of green line shown in Figure 5 and the results of the Rietveld refined reliability suggested the results of Rietveld

refinement was reliable. As listed in Table 2, the cell volume and lattice parameters of $Ca_{0.61}Nd_{0.26}Ti_{1-x}Cr_xO_3$ ceramics increased with increase of Cr substitution at B-site, which was interpreted as a fact that the ionic radius of Cr^{3+} (0.615 Å, CN = 6) is larger than that of Ti^{4+} (0.605 Å, CN = 6). This finding was accordance with the illustration (on the right of Figure 2(a)) that the diffraction peaks for (121) lattice plane shifted towards low angle.

As mentioned before, the P-V-L chemical bond theory has been used widely to explore and establish the relationship between properties and chemical bonds for microwave dielectric ceramics. Thus, this work has used P-V-L theory to obtain bond characteristics. Firstly, a vital premise of successfully used the P-V-L is that the complex crystal formula (polycompound) is decomposed into bonding formula. According to the method propose by Zhang[44], the complex crystals $Ca_{0.61}Nd_{0.26}TiO_3$ could be decomposed into the sum of bonding formula as formula (3) based on the crystal structure and ion occupancy.

$$Ca_{0.61}Nd_{0.26}TiO_3 = Ca_{0.61/12}O1(1)_{0.61/5.22} + Ca_{0.61/12}O1(2)_{0.61/5.22} + Ca_{0.61/12}O1(3)_{0.61/5.22} + Ca_{0.61/12}O1(4)_{0.61/5.22} + Ca_{0.61/6}O2(1)_{0.61/2.61} + Ca_{0.61/6}O2(2)_{0.61/2.61} + Ca_{0.61/6}O2(3)_{0.61/2.61} + Ca_{0.61/6}O2(4)_{0.61/2.61} + Nd_{0.26/12}O1(1)_{0.26/5.22} + Nd_{0.26/12}O1(2)_{0.26/5.22} + Nd_{0.26/12}O1(3)_{0.26/5.22} + Nd_{0.26/12}O1(4)_{0.26/5.22} + Nd_{0.26/6}O2(1)_{0.26/2.61} + Nd_{0.26/6}O2(2)_{0.26/2.61} + Nd_{0.26/6}O2(3)_{0.26/2.61} + Nd_{0.26/6}O2(4)_{0.26/2.61} + Ti_{1/3}O1(1)_{1/3} + Ti_{1/3}O2(1)_{1/3} + Ti_{1/3}O2(2)_{1/3} \quad (3)$$

According to the generalized P–V–L theory[34], the fractional bond ionicity (f_i) of bond μ can be estimated by the series of equations:

$$f_i^{\mu} = \frac{(C^{\mu})^2}{(E_g^{\mu})^2} \quad (4)$$

$$E_g^{\mu} = \sqrt{(E_h^{\mu})^2 + (C^{\mu})^2} \quad (5)$$

$$E_h^{\mu} = \frac{39.74}{(d^{\mu})^{2.48}} \quad (6)$$

$$C^{\mu} = 14.4 b^{\mu} \cdot \exp(-k_s^{\mu} \frac{d^{\mu}}{2}) \left[\frac{(Z_A^{\mu})^*}{d^{\mu}/2} - (n/m)\frac{(Z_B^{\mu})^*}{d^{\mu}/2}\right] \quad (7)$$

where E_g^{μ} is the average energy gap separated into homopolar part $(E_h^{\mu})^2$ and heteropolar part $(C_{\mu})^2$, d^{μ} is distance of individual chemical bond, and b^{μ} is a correction factor. $(Z_A^{\mu})^*$ and $(Z_B^{\mu})^*$ are effective number of valence electrons on the cation and anion, respectively. As reported previously, the lattice energy U can be divided by covalent part U_c^{μ} and ionic part U_i^{μ} of lattice energy for the μ bond:

$$U = \sum_{\mu}(U_c^{\mu} + U_i^{\mu}) \quad (8)$$

U_c^{μ} and U_i^{μ} are given in terms of the ionicity f_i^{μ} and covalency f_c^{μ}:

$$U_c^{\mu} = 2100\mathrm{m}\frac{(Z_+^{\mu})^{1.64}}{(d^{\mu})^{3/4}} f_c^{\mu} \quad (9)$$

$$U_i^{\mu} = 1270\frac{(m+n)Z_+^{\mu}Z^{\mu}}{d^{\mu}}\left(1 - \frac{0.4}{d^{\mu}}\right) f_i^{\mu} \quad (10)$$

where Z_+^{μ} and Z_-^{μ} represent the valence state of Ca^{2+}/Na^{+}, Nd^{3+} and Ti^{4+} cations and O^{2-} anion. Based on the theory of electronegativity and bond energy proposed by Sanderson[45], the bond energy (E) of individual bond μ in a complex crystal could be calculated by these two contributions:

$$E^{\mu} = t_c E_c^{\mu} + t_i E_i^{\mu} \quad (11)$$

where t_c and t_i are the covalent and ionic blending coefficients, E_c^{μ} and E_i^{μ} reflect the energy of the covalent and ionic form, respectively, which could be calculated by following formula:

$$E_c^{\mu} = \frac{r_{cA} + r_{cB}}{d^{\mu}}(E_{A-A}E_{B-B})^{0.5} \quad (12)$$

$$E_i^{\mu} = \frac{33200}{d^{\mu}} \quad (13)$$

where r_{cA} and r_{cB} are the covalent radii, and the bond energy of ions (A representing cation and B representing anion) are obtained from the handbook[46].

All the calculated parameter results of P-V-L theory for $Ca_{0.61}Nd_{0.26}Ti_{1-x}Cr_xO_3$ ceramics were listed in Table S1, Table S2 and Table S3. Figure 6 depicts bond characteristics for $Ca_{0.61}Nd_{0.26}TiO_3$ ceramic. The average bond ionicity of different bonds presents a tendency of Af_i(Ti-O) < Af_i(Ca-O) < Af_i(Nd-O). The relationship of dielectric constant and bond ionicity has been proposed by Batsanov et al[47]. Thus the dielectric constant mainly ascribed

to the bond ionicity of Nd-O bonds for $Ca_{0.61}Nd_{0.26}TiO_3$ ceramic, which would be discussed later in this paper. The lattice energy was regard as a reflection for the crystal stability[48]. As shown in Figure 1, $Ca_{0.61}Nd_{0.26}TiO_3$ crystal was constituted by framework of Ti-O octahedrons, then Ca and Nd ions filled the octahedral interstice. Figure 6(b) presents a following order for lattice energy: AU(Nd-O) < AU(Ca-O) < AU(Ti-O). The high value of lattice energy of Ti-O implied a stable frame in $Ca_{0.61}Nd_{0.26}TiO_3$ crystal. In general, short bond length indicated a high bond energy. As shown in Figure 6(c), the tendency of bond energy was similar with that of bond length for different bonds at B-site.

3.3 Raman spectra and crystal structure analysis

As known, the lattice vibrations could be reflected by Raman spectra. According to the group theory analysis, 24 Raman active modes ($7A_g + 5B_{1g} + 7B_{2g} + 5B_{3g}$) can be expected in $Ca_{0.61}Nd_{0.26}TiO_3$ ceramic (see Table 2). As presented in Figure 1 and Table 2, Ca/Nd ions, Ti atom, O(1) ion and O(2) ion occupied 4c, 4b, 4c and 8d Wyckoff sites with C_s, C_i, C_s, and C_1 site symmetry, respectively. The Ti ions do not contribute to Raman active modes. Wang et al[49]. proposed that each Raman vibrational mode could be regard as a combination of symmetry coordinates under same symmetry. For instance, the all vibrations symmetry coordinates a_g of $Ca_{0.61}Nd_{0.26}TiO_3$ ceramic are sketched in Figure 7, and all of a_g contributed A_g modes based on the results of first-principle calculations. The vibrations symmetry coordinates a_g(1-3) were related to the torsional behavior of the Ti-O octahedrons. a_g(4-5) connected with stretching or bending behavior of the Ti-O bond, and a_g(6-7) were related to the displacements of A-site cations. For every A_g mode, the contribution level of each a_g was different, then this A_g mode would be dependent on the highest contribution level of a_g, subsequently. Similarly, the vibrations symmetry coordinates b_{1g}, b_{2g} and b_{3g} of $Ca_{0.61}Nd_{0.26}TiO_3$ ceramic are shown in Figure S1-S3. It is note-worthy that the frequencies of 24 Raman modes can't be identified precisely just based on vibrations symmetry coordinates.

Actually, there is no relevant literature that has reported the specific frequencies of 24 Raman modes for $Ca_{0.61}Nd_{0.26}TiO_3$ or $CaTiO_3$ ceramic.

The experimental Raman spectra of $Ca_{0.61}Nd_{0.26}Ti_{1-x}Cr_xO_3$ ceramics are shown in Figure 8(a). It is known that many weak peak of Raman modes may be covered up by strong peak or annihilated due to weak signals. So the number of experimental Raman modes is less than that of the predicted Raman modes. Although it is difficult to determine the specific frequencies of each Raman mode in this work, the assignment of observed Raman peaks can be confirmed according to the already published papers[33, 50-52]. As presented in Figure 8 and Table 3, peak at 130 cm^{-1} was related to displacements of A-site cations, and peaks at 130 cm^{-1} and 331 cm^{-1} corresponded to the Ti-O bending modes. The peaks at 130 cm^{-1} and 331 cm^{-1} were dominated by torsional modes, and 677 cm^{-1} was associated with the Ti–O stretching mode. There is no Raman peak at 551 cm^{-1} in pure $CaTiO_3$ and $NdAlO_3$, but a broad band around 551 cm^{-1} occurs in $x$$CaTiO_3$-(1-$x$)$NdAlO_3$ ($0.125 \leq x \leq 0.875$) ceramics[50]. Hence, the Raman peak at 551 cm^{-1} correlated with the 1:1 short range cation ordering at A-site, which has been proposed by Fu's study[52]. Figure 8(b) shows the Raman spectrum of TiO_2. As discussed above, the second phase TiO_2 was detected as $x = 0.015$. The effect of TiO_2 on Raman spectra of $Ca_{0.61}Nd_{0.26}Ti_{1-x}Cr_xO_3$ ceramics can be negligible. As shown in Figure 8(a), the Raman peak at 765 cm^{-1} with $x = 0$ move to 775 cm^{-1}, and become strong with increase of substituted quantity of Cr. This result can be explained by cation ordering at B-site[50, 52, 53]. Whereas this cation ordering was deemed as a short range order (SRO), and this SRO effects enhanced as Cr content increased, which was characterized by intensity of Raman peak at 775 cm^{-1}. On the other hand, in $Ca_{0.61}Nd_{0.26}Ti_{1-x}Cr_xO_3$ system, Cr^{3+} and Ti^{4+} occupied randomly the B sites in $Ca_{0.61}Nd_{0.26}TiO_3$ crystal. Although SRO existed, there showed a disordering at B-site as a whole. Due to the differences of ionic sizes, electrovalence and force constants between Cr^{3+} and Ti^{4+}, there were non-equivalent Ti/Cr-O octahedrons, indicating a possible appearance of active Raman mode. Therefore, this may contribute to the Raman peak at 775 cm^{-1}.

As previously mentioned, the $Ca_{0.61}Nd_{0.26}TiO_3$ crystal was a basic framework made of Ti-O octahedrons, and Ca and Nd fill the octahedral interstice as shown in Figure 1. Furthermore, the contrast of ideal cubic perovskite with orthorhombic perovskite is given in Figure 9. The tilted Ti-O octahedrons played a significant role in $Ca_{0.61}Nd_{0.26}TiO_3$ crystal, especially dielectric properties. Hence, we calculated the parameters to assess the stability of framework structure. The bond strength ($S_{(B-O)}$) for B-site and B-O octahedron distortion (δ_{oct}) were calculated using equations (14) and (15), respectively.

$$S_{(B-O)} = \sum s_0 (R_i/R_0)^{-N} \quad (14)$$

Here s_0, R_0 and N are the universal bond strength parameters, R_i is the bond length for individual bond at B-site.

$$\delta_{oct} = \frac{1}{6}\sum(\frac{R_i-\bar{R}}{\bar{R}})^2 \quad (15)$$

Here R_i is the bond length for individual bond at B-site and $\bar{R}$ is the average value for six B-O bond length. Figure 10 shows the tendency of relative four parameters as Cr content increase. As x value increased, the B-site bond energy and bond strength decrease continuously and the oxygen octahedron distortion increase as shown in Figure 10(a). Also Table 1 gives the increasing trend of B-site bond length and Figure 10(b) presents the declined trend of lattice energy for Ca-O, Nd-O and Ti/Cr-O bonds as a function of x values. These results proved that the oxygen octahedrons' framework stability was disturbed and decreased. This perturbation was tiny, while it would have impacts on the dielectric properties.

3.4. Dielectric characteristics

Table 4 lists the microwave dielectric properties of $Ca_{0.61}Nd_{0.26}Ti_{1-x}Cr_xO_3$ ($0 \leq x \leq 0.03$) samples sintered at different temperatures. The tendency of these data and factors influencing dielectric properties will be discussed later in this paper.

Based on the collected data of bulk density (ρ_{bulk}) for $Ca_{0.61}Nd_{0.26}Ti_{1-x}Cr_xO_3$ ceramics, the relative density can be calculated through this formula:

$$\rho_{rel} = \frac{\rho_{bulk}}{\rho_{the}} = \frac{\rho_{bulk}}{nm_A/(V_{cell}N_A)} \quad (16)$$

Where m_A is the atomic weight; V_{cell} is the unit cell volume; n is the number of atoms in each unit cell and N_A is the Avogadro's number. Figure S4(b) shows the dielectric constant values of $Ca_{0.61}Nd_{0.26}Ti_{1-x}Cr_xO_3$ ($0 \le x \le 0.03$) ceramics sintered at different temperatures. Clearly, the sintering temperature had little effect on the dielectric constant, but the doping Cr contents had a great influence on the dielectric constant for $Ca_{0.61}Nd_{0.26}Ti_{1-x}Cr_xO_3$ ($0 \le x \le 0.03$) ceramics. Figure 11 presents dielectric constant (ε_r), relative density and bond ionicity f_i of different bond a function of x value for $Ca_{0.61}Nd_{0.26}Ti_{1-x}Cr_xO_3$ ceramics sintered at1400 ºC. As shown in Figure 11(a), the dielectric constant decreased from about 107 with x = 0 to about 86 with x = 0.03, and the relative densities of all composition were over 95% but presented a descending trend as a whole. The second phase TiO_2 was confirmed that it had no influence on the decrease of dielectric constant for $Ca_{0.61}Nd_{0.26}Ti_{1-x}Cr_xO_3$ ceramics owing to its ε_r value of 104[54]. As shown in Figure 3, there were more grain boundary defects when grain size decreased as doping Cr content increased. This situation of decrease for grain size not only lowered the relative densities (increased porosity) but dielectric constant. This should be considered to be of extrinsic nature[55]. It can be understood by the existence of more-or-less universal (grain-size independent) low-permittivity grain-boundary layer (dead layer), the grain core sustaining the bulk material properties. These dead layers deteriorated the dielectric constant. On the other hand, Batsanov et al[47]. proposed a mathematical relationship: $\varepsilon = (n^2-1)/(1-f_i)+1$, which indicated that the dielectric constant was positively correlated with bond ionicity. Where n represents the refractive index. Figure 11(b) depicts a downward trend of f_i value as Cr content increase for each bond, reflecting a downward trend of dielectric constant with increase of Cr content for $Ca_{0.61}Nd_{0.26}Ti_{1-x}Cr_xO_3$ ceramics. On the other hand, the theoretical ionic polarizability was considered as a significant internal factor affecting dielectric constant for solid solutions. The Cr^{3+} has a lower ionic polarizability value of 1.45 $Å^3$ than

that value of 2.93 $Å^3$ for Ti^{4+}, which is responsible for decline of dielectric constant as Cr concentration increases.

The τ_f value is affected by many factors such as structure, second phase. Figure S4(a) shows the τ_f values of $Ca_{0.61}Nd_{0.26}Ti_{1-x}Cr_xO_3$ ($0 \le x \le 0.03$) ceramics sintered at different temperatures. Obviously, the τ_f values, similar to dielectric constant, rarely depended on the sintering temperature. Figure 12 shows the variation of $Ca_{0.61}Nd_{0.26}Ti_{1-x}Cr_xO_3$ ceramics τ_f value as a function of *x* value. In this work, the TiO_2 phase should be excluded for investigating effects on the τ_f value in $Ca_{0.61}Nd_{0.26}Ti_{1-x}Cr_xO_3$ ceramics, because of τ_f value of 400 ppm/ºC for TiO_2. As is well known that the τ_f value has a close relationship with temperature coefficient of dielectric constant (τ_ε), which is given in equation (17).

$$\tau_f = -(\frac{\tau_\varepsilon}{2} + \alpha_L) \quad (17)$$

Where α_L is the thermal expansion coefficient and a positive constant for $Ca_{0.61}Nd_{0.26}Ti_{1-x}Cr_xO_3$ ceramics. Additionally, the mathematical expression calculating the τ_ε value has been proposed by Colla et al[56], and is shown in equation (18).

$$\tau_\varepsilon = \frac{(\varepsilon-1)(\varepsilon+2)}{\varepsilon}(A + B + C) \quad (18)$$

Here ε is the dielectric constant, $A = \frac{1}{\alpha_m}(\frac{\partial \alpha_m}{\partial T})_V$, $B = \frac{1}{\alpha_m}\left(\frac{\partial \alpha_m}{\partial V}\right)_T (\frac{\partial V}{\partial T})_P$, and $C = -\frac{1}{V}(\frac{\partial V}{\partial T})_P$. As shown above, α_m is the polarizability, and *V* denotes the volume. Generally, term *A* represents the dependence of the polarizability on temperature, and is negative. For $Ca_{0.61}Nd_{0.26}Ti_{1-x}Cr_xO_3$ ceramics, the value of $|A|$ decrease with increase of Cr content due to the lower ionic polarizability value of Cr^{3+} than that of Ti^{4+}. Term *B* can be seen as a changeless positive value, and just become negative when $(\partial V/\partial T)_P$ is negative. Term *C* is negative and $|C| \approx 3\alpha_L$. Taken together, the τ_f value was dependent on the term *B*, and it was obvious to infer τ_f value decreased as *x* value increased referring to the equation (17) in $Ca_{0.61}Nd_{0.26}Ti_{1-x}Cr_xO_3$ ceramics.

The dielectric loss is a crucial parameter for dielectric microwave ceramics and their applications. Many factors have been confirmed to affect the dielectric loss. The bulk density, other phases, grain growth, etc were classified as external factors. Also the crystal defects, lattice vibrations, phase transition, etc were deemed to the internal factors. The quality factor (Q×f) was usually assessed the dielectric loss instead of tanδ for dielectric microwave ceramics. Figure 13 presents the Q×f values of $Ca_{0.61}Nd_{0.26}Ti_{1-x}Cr_xO_3$ ceramics. As shown in Figure 13(a), the Q×f value depended on the sintering temperature for the samples with same components. To investigated this result, the SEM images of $Ca_{0.61}Nd_{0.26}Ti_{1-x}Cr_xO_3$ (x = 0.01) ceramics sintered at different temperatures were obtained and presented in Figure 14. As sintering temperature increased from 1350 ºC to 1400 ºC, the grain size increased and the microstructure became more compact. Nevertheless, the grain boundaries became blurred when the sintering temperature increased to 1450 ºC, which deteriorated the Q×f value. The $Ca_{0.61}Nd_{0.26}Ti_{1-x}Cr_xO_3$ (x = 0.01) ceramics presented the maximum Q×f value at 1400 ºC. Besides, Figure 13(b) gives a tendency that the Q×f value increase initially, and reach the maximum of 16,078 GHz, then decrease as x value increase. This result implied that the introducing Cr into $Ca_{0.61}Nd_{0.26}TiO_3$ ceramic was in favor of improvement of Q×f value. As introduced in previous section, it was easy to produce oxygen vacancies at high sintering temperatures for $Ca_{0.61}Nd_{0.26}TiO_3$ ceramic, resulting in Ti^{3+}. When Ti was substituted by Cr, there was a reaction during the high temperature sintering process as following:

$$Cr_2O_3 + 1.22CaO + 0.26Nd_2O_3 \xrightarrow{2Ca_{0.61}Nd_{0.26}TiO_3} 2Cr'_{Ti} + V_O^{\cdot\cdot} + 1.22Ca_{Ca}^{\times} + 0.52Nd_{Nd}^{\times} + 5O_O^{\times} \quad (19)$$

As shown in reaction (1,2,19), the generation of oxygen vacancies in reaction (19) would restrain that of in reaction (1), then the generation of the unbound electrons were cut off. The reduction of Ti^{4+} was suppressed subsequently. The XPS analysis was carried out to determine valence states of Ti in $Ca_{0.61}Nd_{0.26}Ti_{1-x}Cr_xO_3$ ceramics, and the Ti2p XPS spectra and that of fitting curve are presented in Figure 15. The peak of Ti^{3+} 2p3/2 located at 457.8 eV. The peak of Ti^{4+} 2p3/2 increased from 458.3 eV at x = 0 to 458.7 eV at x = 0.01, then

remained unchanged. Meanwhile the valence state of +3 for Ti was detected at x = 0, 0.005 using Gaussian-Lorentz fitting. Therefore, the Ti^{3+} was eliminated by acceptor dopant of Cr with $x \geq 0.01$, which was responsible for the fact that the Q×f value increase initially, and reach the maximum at $x = 0.01$. When $x \geq 0.015$, the excess oxygen vacancies were introducing into the $Ca_{0.61}Nd_{0.26}TiO_3$ crystal, the conduction loss would have a relatively large impact on the Q×f value. According to the previous structure analysis, the stability of structure decreased with increase of Cr content. Considering these two points, the Q×f value declined continuously with $x \geq 0.015$.

As discussed above, the balanced amount of trivalent Cr as an acceptor dopant contributed to the suppression of reduction reaction for Ti^{4+}. It was a desirable way to enhance the Q×f value for $Ca_{0.61}Nd_{0.26}TiO_3$ ceramic, even other Ti-based ceramics sintered at high temperatures.

4. Conclusion

In the present work, the $Ca_{0.61}Nd_{0.26}Ti_{1-x}Cr_xO_3$ ($0 \leq x \leq 0.03$) ceramics prepared by solid-state reaction were explored to investigate the effects of Cr substitution for Ti at B-site on the structure and microwave dielectric properties. The XRD patterns showed the second phase TiO_2 appeared when $x \geq 0.015$, while this existence had no impact on the microwave dielectric properties for $Ca_{0.61}Nd_{0.26}Ti_{1-x}Cr_xO_3$ ceramics. The SEM images demonstrated that Cr played a role in restraining grain growth for $Ca_{0.61}Nd_{0.26}TiO_3$ ceramic. The SRO was verified by Raman spectra. As Cr concentration increased, the dielectric constant and τ_f value declined, which was related to the average f_i value and the ionic polarizability in $Ca_{0.61}Nd_{0.26}Ti_{1-x}Cr_xO_3$ ceramics. The decrease of grain size aslo was responsible for the decline of dielectric constant. Furthermore, the balanced amount of trivalent Cr as an acceptor dopant contributed to the suppression of reduction reaction for Ti^{4+}, leading to the improvement of the Q×f value for $Ca_{0.61}Nd_{0.26}TiO_3$ ceramic. When $x \geq 0.015$, introducing the excess oxygen vacancies into the $Ca_{0.61}Nd_{0.26}TiO_3$ crystal would deteriorated the Q×f value.

ACKNOWLEDGEMENTS

This work was supported by the National Natural Science Foundation of China (Grant No. 51672038).

REFERENCES

[1] F. Luo, B. Tang, Y. Yuan, Z. Fang, S. Zhang, Microstructure and microwave dielectric properties of $Na_{1/2}Sm_{1/2}TiO_3$ filled PTFE, an environmental friendly composites, Appl. Surf. Sci. 436 (2018) 900-906.

[2] Z. Fang, B. Tang, Y. Yuan, X. Zhang, S. Zhang, Structure and microwave dielectric properties of the $Li_{2/3(1-x)}Sn_{1/3(1-x)}Mg_xO$ systems (x = 0-4/7), J. Am. Ceram. Soc. 101 (2018) 252-264.

[3] M.T. Sebastian, Dielectric materials for wireless communication. 2010: Elsevier.

[4] X. Zhang, B. Tang, Z. Fang, H. Yang, Z. Xiong, L. Xue, S. Zhang, Structural evolution and microwave dielectric properties of a novel $Li_3Mg_{2-x/3}Nb_{1-2x/3}Ti_xO_6$ system with a rock salt structure, Inorg Chem Front. 5 (2018) 3113-3125.

[5] D. Zhou, L.-X. Pang, D.-W. Wang, Z.-M. Qi, I.M. Reaney, High Quality Factor, Ultralow Sintering Temperature $Li_6B_4O_9$ Microwave Dielectric Ceramics with Ultralow Density for Antenna Substrates, ACS Sustain Chem Eng. 6 (2018) 11138-11143.

[6] D. Zhou, J. Li, L.-X. Pang, D.-W. Wang, I.M. Reaney, Novel water insoluble $(Na_xAg_{2-x})MoO_4$ ($0 \leq x \leq 2$) microwave dielectric ceramics with spinel structure sintered at 410 degrees, J. Mater. Chem. C. 5 (2017) 6086-6091.

[7] H.-H. Guo, D. Zhou, L.-X. Pang, Z.-M. Qi, Microwave dielectric properties of low firing temperature stable scheelite structured $(Ca,Bi)(Mo,V)O_4$ solid solution ceramics for LTCC applications, J. Eur. Ceram. Soc. 39 (2019) 2365-2373.

[8] D. Zhou, J. Li, L.-X. Pang, G.-H. Chen, Z.-M. Qi, D.-W. Wang, I.M. Reaney, Crystal Structure, Infrared Spectra, and Microwave Dielectric Properties of Temperature-Stable Zircon-Type $(Y,Bi)VO_4$ Solid-Solution Ceramics, ACS Omega. 1 (2016) 963-970.

[9] Z. Xiong, B. Tang, C. Yang, C. Yuan, S. Zhang, Different Additives Doped Ca–Nd–Ti Microwave Dielectric Ceramics with Distorted Oxygen Octahedrons and High Q × f Value, ACS Omega. 3 (2018) 11033-11040.

[10] R. Lowndes, F. Azough, R. Cernik, R. Freer, Structures and microwave dielectric properties of $Ca_{(1-x)}Nd_{2x/3}TiO_3$ ceramics, J. Eur. Ceram. Soc. 32 (2012) 3791-3799.

[11] Y. Masashi, H. Naoki, T. Takahiro, S. Akira, Structure and Dielectric Properties of $(Ca_{1-x}Nd_{2x/3})TiO_3$, Jpn. J. Appl. Phys. 36 (1997) 6818.

[12] T. Hisakazu, B. Yoko, E. Kenichi, S. Kenichi, Microwave Dielectric Properties and Crystal Structure of $CaO–Li_2O–(1-x)Sm_2O_3–xLn_2O_3–TiO_2$ (Ln: lanthanide) Ceramics System, Jpn. J. Appl. Phys. 35 (1996) 5069.

[13] M. Jong Ha, M.J. Hyun , S.P. Hyun , Y.S. Jong , S.K. Ho Sintering Behavior and Microwave Dielectric Properties of (Ca, La)(Ti, Al)O_3 Ceramics, Jpn. J. Appl. Phys. 38 (1999) 6821.

[14] W.S. Kim, E.S. Kim, K.H. Yoon, Effects of Sm^{3+} substitution on dielectric properties of $Ca_{1-x}Sm_{2x/3}TiO_3$ ceramics at microwave frequencies, J. Am. Ceram. Soc. 82 (1999) 2111-2115.

[15] H. Jantunen, R. Rautioaho, A. Uusimäki, S. Leppävuori, Compositions of $MgTiO_3–CaTiO_3$ ceramic with two borosilicate glasses for LTCC technology, J. Eur. Ceram. Soc. 20 (2000) 2331-2336.

[16] C.-H. Hsu, H.-A. Ho, Microwave dielectric in the $Sm(Co_{1/2}Ti_{1/2})O_3–CaTiO_3$ ceramic system with near-zero temperature coefficient with resonant frequency, Mater. Lett. 64 (2010) 396-398.

[17] D.L. Cairns, I.M. Reaney, N. Otten, D. Iddles, T. Price, Structural determination and microwave properties of

(x)Re($Co_{1/2}Ti_{1/2}$)O_3–(1−x)$CaTiO_3$ (Re=La and Nd) solid solutions, J. Eur. Ceram. Soc. 26 (2006) 875-882.

[18] E.A. Nenasheva, L.P. Mudroliubova, N.F. Kartenko, Microwave dielectric properties of ceramics based on $CaTiO_3$–$LnMO_3$ System (Ln–La, Nd; M–Al, Ga), J. Eur. Ceram. Soc. 23 (2003) 2443-2448.

[19] A. Yokoi, H. Ogawa, A. Kan, H. Ohsato, Y. Higashida, Microwave dielectric properties of $Mg_4Nb_2O_9$–3.0wt.% LiF ceramics prepared with $CaTiO_3$ additions, J. Eur. Ceram. Soc. 25 (2005) 2871-2875.

[20] D. Wang, S. Zhang, G. Wang, Y. Vardaxoglou, W. Whittow, D. Cadman, D. Zhou, et al., Cold sintered $CaTiO_3$-K_2MoO_4 microwave dielectric ceramics for integrated microstrip patch antennas, Appl Mater Today. 18 (2020) 100519.

[21] I.-S. Kim, W.-H. Jung, Y. Inaguma, T. Nakamura, M. Itoh, Dielectric properties of a-site deficient perovskite-type lanthanum-calcium-titanium oxide solid solution system [(1−x)$La_{2/3}TiO_3$−x$CaTiO_3$ ($0.1 \leq x \leq 0.96$)], Mater. Res. Bull. 30 (1995) 307-316.

[22] H. Chen, B. Tang, P. Fan, S. Duan, M. Wei, Y. Yuan, S. Zhang, Microwave dielectric properties of aluminum substituted $Ca_{0.61}Nd_{0.26}TiO_3$ ceramics, J. Ceram. Soc. Jpn. 124 (2016) 903-906.

[23] H. Chen, C. Huang, Microwave Dielectric Properties and Microstructures of $Ca_{1-x}Nd_{2x/3}TiO_3$–$Li_{1/2}Nd_{1/2}TiO_3$ Ceramics, Jpn. J. Appl. Phys. 41 (2002) 5650.

[24] M. Hu, H. Gu, X. Chu, J. Qian, Z. Xia, Crystal structure and dielectric properties of (1−x)$Ca_{0.61}Nd_{0.26}TiO_3$+x$Nd(Mg_{1/2}Ti_{1/2})O_3$ complex perovskite at microwave frequencies, J. Appl. Phys. 104 (2008) 124104.

[25] A. Templeton, X. Wang, S.J. Penn, S.J. Webb, L.F. Cohen, N.M. Alford, Microwave Dielectric Loss of Titanium Oxide, J. Am. Ceram. Soc. 83 (2000) 95-100.

[26] R.C. Pullar, S.J. Penn, X. Wang, I.M. Reaney, N.M. Alford, Dielectric loss caused by oxygen vacancies in titania ceramics, J. Eur. Ceram. Soc. 29 (2009) 419-424.

[27] B. Tang, S. Yu, H. Chen, S. Zhang, X. Zhou, The influence of Cu substitution on the microwave dielectric properties of $BaZn_2Ti_4O_{11}$ ceramics, J. Alloys. Compd. 551 (2013) 463-467.

[28] X. Yao, H. Lin, W. Chen, L. Luo, Anti-reduction of Ti^{4+} in $Ba_{4.2}Sm_{9.2}Ti_{18}O_{54}$ ceramics by doping with MgO, $Al2O_3$ and MnO_2, Ceram. Int. 38 (2012) 3011-3016.

[29] B. Huang, X. Lu, Y. Zhang, L. Wang, Z. Fu, Z. Wang, Q. Zhang, The formation of “dark holes” and their significant influences on microwave dielectric properties of $Ba_{4.2}Nd_{9.2}Ti_{18}O_{54}$ ceramics, Mater Charact. 111 (2016) 81-85.

[30] Z. Xiong, B. Tang, X. Zhang, C. Yang, S. Zhang, Suppression of Ti^{3+} generation in $Ba_{3.75}Nd_{9.5}Ti_{17.5}M_{0.5}O_{54}$ (M = Cu, Cr, Al, Mn) ceramics, Ceram. Int. 44 (2018) 19058-19062.

[31] Z. Xiong, B. Tang, Z. Fang, C. Yang, S. Zhang, Crystal structure, Raman spectroscopy and microwave dielectric properties of $Ba_{3.75}Nd_{9.5}Ti_{18-z}(Al_{1/2}Nb_{1/2})_zO_{54}$ ceramics, J. Alloys. Compd. 723 (2017) 580-588.

[32] Z. Fang, B. Tang, E. Li, S. Zhang, High-Q microwave dielectric properties in the $Na_{0.5}Sm_{0.5}TiO_3$+Cr_2O_3 ceramics by one synthetic process, J. Alloys. Compd. 705 (2017) 456-461.

[33] R. Lowndes, M. Deluca, F. Azough, R. Freer, Probing structural changes in $Ca_{(1-x)}Nd_{2x/3}TiO_3$ ceramics by Raman spectroscopy, J. Appl. Phys. 113 (2013) 044115.

[34] B.F. Levine, Bond susceptibilities and ionicities in complex crystal structures, J. Phys. Chem. Phys. 59 (1973) 1463-1486.

[35] B. Tang, Q. Xiang, Z. Fang, X. Zhang, Z. Xiong, H. Li, C. Yuan, et al., Influence of Cr^{3+} substitution for Mg^{2+} on the crystal structure and microwave dielectric properties of $CaMg_{1-x}Cr_{2x/3}Si_2O_6$ ceramics, Ceram. Int. 45 (2019) 11484-11490.

[36] B. Tang, Q. Xiang, Z. Fang, X. Guo, S. Zhang, Microwave dielectric properties of $Ba_{3.75}Nd_{9.5}Ti_{18-z}Cr_{4z/3}O_{54}$ ceramics, 29 (2018) 535-540.

[37] V.M. Ferreira, F. Azough, R. Freer, J.L. Baptista, The effect of Cr and La on $MgTiO_3$ and $MgTiO_3$–$CaTiO_3$ microwave dielectric ceramics, J. Mater. Res. 12 (1997) 3293-3299.

[38] X. Guo, B. Tang, J. Liu, H. Chen, S. Zhang, Microwave dielectric properties and microstructure of $Ba_{6-3x}Nd_{8+2x}Ti_{18-y}(Cr_{1/2}Nb_{1/2})_yO_{54}$ ceramics, J. Alloys. Compd. 646 (2015) 512-516.

[39] M.S. Fu, X.Q. Liu, X.M. Chen, Structure and microwave dielectric characteristics of $Ca_{1-x}Nd_{2x/3}TiO_3$ ceramics, J. Eur. Ceram. Soc. 28 (2008) 585-590.

[40] A. Glazer, Simple ways of determining perovskite structures, Acta. Crystallogr. A. 31 (1975) 756-762.

[41] R.B. Atkin, R.M. Fulrath, Point Defects and Sintering of Lead Zirconate-Titanate, J. Am. Ceram. Soc. 54 (1971) 265-270.

[42] Y.D. Hou, P.X. Lu, M.K. Zhu, X.M. Song, J.L. Tang, B. Wang, H. Yan, Effect of Cr_2O_3 addition on the structure and electrical properties of $Pb((Zn_{1/3}Nb_{2/3})_{0.20}(Zr_{0.50}Ti_{0.50})_{0.80})O_3$ ceramics, Mater. Sci. Eng. B. 116 (2005) 104-108.

[43] H.H. Hng, P.L. Chan, Cr_2O_3 doping in ZnO–0.5mol% V_2O_5 varistor ceramics, Ceram. Int. 35 (2009) 409-413.

[44] S. Zhang, Investigation of chemical bonds on complex crystals, Chinese J Chem Phys. 4 (1991) 109-115.

[45] R.T. Sanderson, Electronegativity and bond energy, J. Am. Chem. Soc. 105 (1983) 2259-2261.

[46] Y.-R. Luo, Comprehensive handbook of chemical bond energies. 2007: CRC press.

[47] S.S. Batsanov, Dielectric Methods of Studying the Chemical Bond and the Concept of Electronegativity, Russ. Chem. Rev+. 51 (1982) 684-697.

[48] D. Liu, S. Zhang, Z. Wu, Lattice Energy Estimation for Inorganic Ionic Crystals, Inorg. Chem. 42 (2003) 2465-2469.

[49] C.-H. Wang, X.-P. Jing, L. Wang, J. Lu, XRD and Raman Studies on the Ordering/Disordering of $Ba(Mg_{1/3}Ta_{2/3})O_3$, 92 (2009) 1547-1551.

[50] H. Zheng, I.M. Reaney, G.D.C.C. de Györgyfalva, R. Ubic, J. Yarwood, M.P. Seabra, V.M. Ferreira, Raman spectroscopy of $CaTiO_3$-based perovskite solid solutions, J. Mater. Res. 19 (2004) 488-495.

[51] Y. Li, S. Qin, F. Seifert, Phase transitions in A-site substituted perovskite compounds: The $(Ca_{1-2x}Na_xLa_x)TiO_3$ ($0 \leqslant x \leqslant 0.5$) solid solution, J. Solid. State. Chem. 180 (2007) 824-833.

[52] M.S. Fu, X.Q. Liu, X.M. Chen, Raman spectra analysis for $Ca(B_{1/3}'B_{2/3}'')O_3$-based complex perovskite ceramics, 104 (2008) 104108.

[53] H. Zheng, G.D.C. Csete de Györgyfalva, R. Quimby, H. Bagshaw, R. Ubic, I.M. Reaney, J. Yarwood, Raman spectroscopy of B-site order–disorder in $CaTiO_3$-based microwave ceramics, J. Eur. Ceram. Soc. 23 (2003) 2653-2659.

[54] D.-W. Kim, J.-H. Kim, J.-R. Kim, K.-S. Hong, Phase Constitutions and Microwave Dielectric Properties of $Zn_3Nb_2O_8$–TiO_2, Jpn. J. Appl. Phys. 40 (2001) 5994-5998.

[55] J. Petzelt, Dielectric Grain-Size Effect in High-Permittivity Ceramics, Ferroelectr. 400 (2010) 117-134.

[56] E.L. Colla, I.M. Reaney, N. Setter, Effect of structural changes in complex perovskites on the temperature coefficient of the relative permittivity, J. Appl. Phys. 74 (1993) 3414-3425.

Table 1. Crystallographic data obtained from Rietveld refinement for $Ca_{0.61}Nd_{0.26}Ti_{1-x}Cr_xO_3$ ($0 \leq x \leq 0.03$) ceramics sintered at1400 ºC.

x (mol)	0	0.005	0.01	0.015	0.02	0.025	0.03
a (Å)	5.4386	5.4392	5.4411	5.4418	5.4426	5.4434	5.4436
b (Å)	7.6655	7.6682	7.6696	7.6701	7.6708	7.6712	7.6716
c (Å)	5.4079	5.4095	5.4105	5.4110	5.4122	5.4130	5.4133
V_{cell} (Å^3)	225.4531	225.6242	225.7859	225.8505	225.9545	226.0326	226.0658
R_{wp} (%)	5.25	6.83	5.97	6.13	5.64	5.24	6.29
R_p (%)	3.75	4.96	5.07	4.67	4.27	4.01	4.7
χ^2	1.64	1.669	1.766	1.269	1.098	1.017	1.419
TiO_2 (*wt.*%)	0	0	0	1.23	1.72	1.96	2.48
Ca/Nd-O(1)^1 (Å)	2.3807	2.3813	2.3819	2.3825	2.3833	2.3845	2.3858
Ca/Nd-O(1)^2 (Å)	2.5438	2.5445	2.5453	2.5459	2.5468	2.5473	2.5479
Ca/Nd-O(1)^3 (Å)	2.9734	2.9739	2.9744	2.9752	2.9759	2.9768	2.9779
Ca/Nd-O(1)^4 (Å)	3.0862	3.0874	3.0882	3.0897	3.0904	3.0919	3.0928
Ca/Nd-O(2)^1 ×2 (Å)	2.4611	2.4623	2.4633	2.4643	2.4652	2.4663	2.4671
Ca/Nd-O(2)^2 ×2 (Å)	2.6563	2.6569	2.6575	2.6582	2.6589	2.6596	2.6606
Ca/Nd-O(2)^3 ×2 (Å)	2.6781	2.6793	2.6799	2.6804	2.6813	2.6819	2.6827
Ca/Nd-O(2)^4 ×2 (Å)	3.1176	3.1186	3.1194	3.1202	3.1211	3.1223	3.1234
Ti/Cr-O(1)^1 ×2 (Å)	1.9543	1.9581	1.9604	1.9654	1.9674	1.9684	1.9688
Ti/Cr-O(2)^1 ×2 (Å)	1.9109	1.9112	1.9123	1.9127	1.9136	1.9142	1.9146
Ti/Cr-O(2)^2 ×2 (Å)	1.9756	1.9799	1.9849	1.9889	1.9935	1.9985	2.0013

Table 2. Mechanical representation for each one of the Wyckoff positions in $Ca_{0.61}Nd_{0.26}TiO_3$ ceramic with Pnma space group.

Atom	Wyckoff notation	Site symmetry	Irreducible representations
Ca/Nd	4c	C_s	$2A_g + B_{1g} + 2B_{2g} + B_{3g} + A_u + 2B_{1u} + B_{2u} + 2B_{3u}$
Ti	4b	C_i	$3A_u + 3B_{1u} + 3B_{2u} + 3B_{3u}$
O1	4c	C_s	$2A_g + B_{1g} + 2B_{2g} + B_{3g} + A_u + 2B_{1u} + B_{2u} + 2B_{3u}$
O2	8d	C_1	$3A_g + 3B_{1g} + 3B_{2g} + 3B_{3g} + 3A_u + 3B_{1u} + 3B_{2u} + 3B_{3u}$
$\Gamma_{Raman} = 7A_g + 5B_{1g} + 7B_{2g} + 5B_{3g}$			
$\Gamma_{IR} = 9B_{1u} + 7B_{2u} + 9B_{3u}$			
$\Gamma_{silent} = 8A_u + 7B_{2u} + 9B_{3u}$			
$\Gamma_{acoustic} = B_{1u} + B_{2u} + B_{3u}$			

Table 3. Observed frequencies and classification of the Raman-active modes in $Ca_{0.61}Nd_{0.26}Ti_{1-x}Cr_xO_3$ ($0 \le x \le 0.03$) ceramics.

Assignments	0	0.005	0.01	0.015	0.02	0.025	0.03
Displacements of A-site cations	130	132	128	130	131	132	131
Ti-O bending modes	233	233	232	234	235	233	233
	331	332	331	333	331	333	332
Torsional modes	453	453	453	453	453	453	453
	470	471	472	471	473	471	472
Short range ordering at A-site	551	551	552	551	553	551	552
Ti–O stretching mode	677	678	677	679	676	677	678
	765	-	-	-	-	-	-
Short range ordering at B-site	-	775	775	776	775	775	776

Table 4. The microwave dielectric properties of $Ca_{0.61}Nd_{0.26}Ti_{1-x}Cr_xO_3$ ($0 \le x \le 0.03$) samples sintered at different temperatures.

	ST (ºC)	0	0.005	0.01	0.015	0.02	0.025	0.03
ε_r	1350	106.2	102.5	98.6	95.4	92.1	88.4	85.9
	1375	106.5	102.4	99.1	95.8	92.7	88.5	86.3
	1400	106.8	102.7	99.3	96.2	92.8	88.3	86.1
	1425	107.2	102.8	98.9	96.0	92.4	88.2	85.7
	1450	106.3	102.5	98.7	95.2	92.0	87.7	85.5
Q×f (GHz)	1350	10233	12079	15414	12677	10623	9423	8714
	1375	11397	13512	15732	12523	11148	9678	8423
	1400	11425	13394	16078	12937	10985	9439	8671
	1425	10834	13215	15259	11782	10361	9562	8593
	1450	9687	11643	14236	11043	9982	9104	8244
τ_f (ppm/ºC)	1350	268.6	262.4	245.1	233.2	215.9	203.2	199.3
	1375	270.5	260.7	243.1	231.4	214.7	204.4	200.6
	1400	271.3	261.2	244.5	233.9	215.3	204.6	198.8
	1425	270.6	259.4	245.6	232.8	216.0	205.6	199.7
	1450	271.2	261.6	242.5	233.3	213.8	203.9	199.5

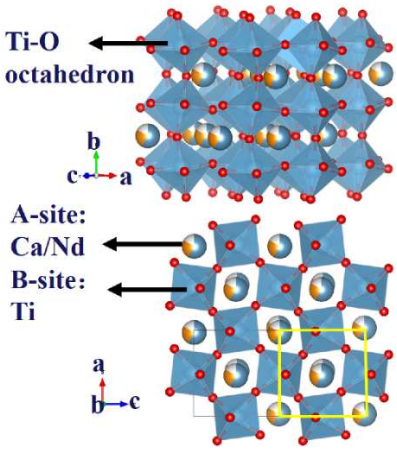

Figure 1. Schematic diagram of the orthorhombic perovskite $Ca_{0.61}Nd_{0.26}TiO_3$ crystal structure.

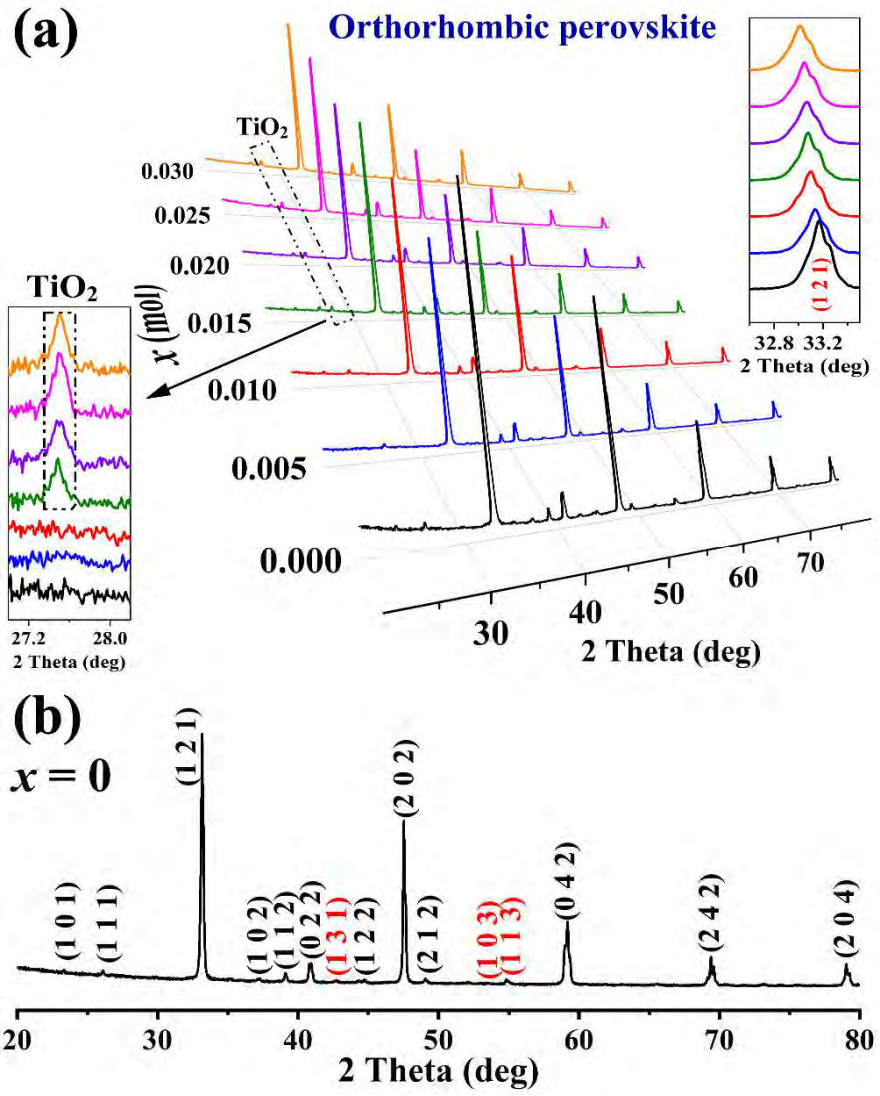

Figure 2. (a) Powder X-ray diffraction patterns of $Ca_{0.61}Nd_{0.26}Ti_{1-x}Cr_xO_3$ ($0 \le x \le 0.03$) ceramics sintered at 1400 ºC; (b) The indices of lattice planes for $Ca_{0.61}Nd_{0.26}TiO_3$ ceramic.

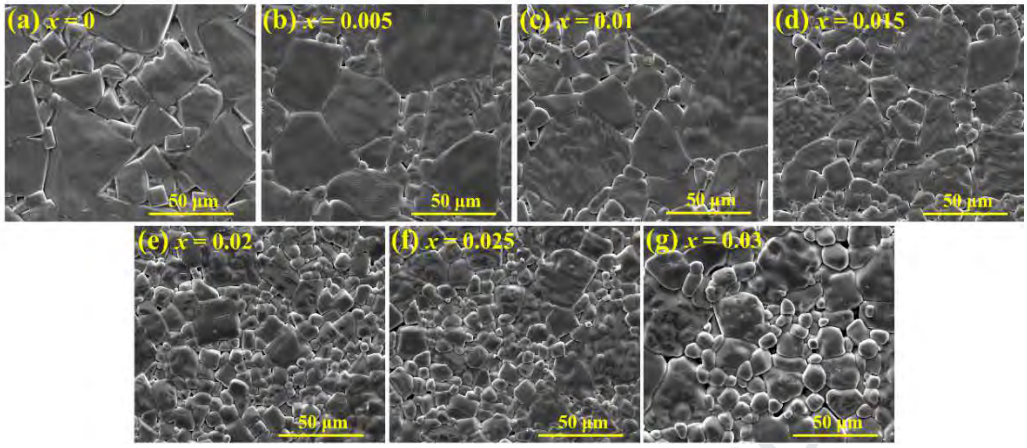

Figure 3. SEM images of $Ca_{0.61}Nd_{0.26}Ti_{1-x}Cr_xO_3$ ($0 \leq x \leq 0.03$) ceramics sintered at 1400 ºC with (a) x = 0; (b) x = 0.005; (c) x =0.01; (d) x = 0.015; (e) x = 0.02; (f) x = 0.025; (g) x = 0.03.

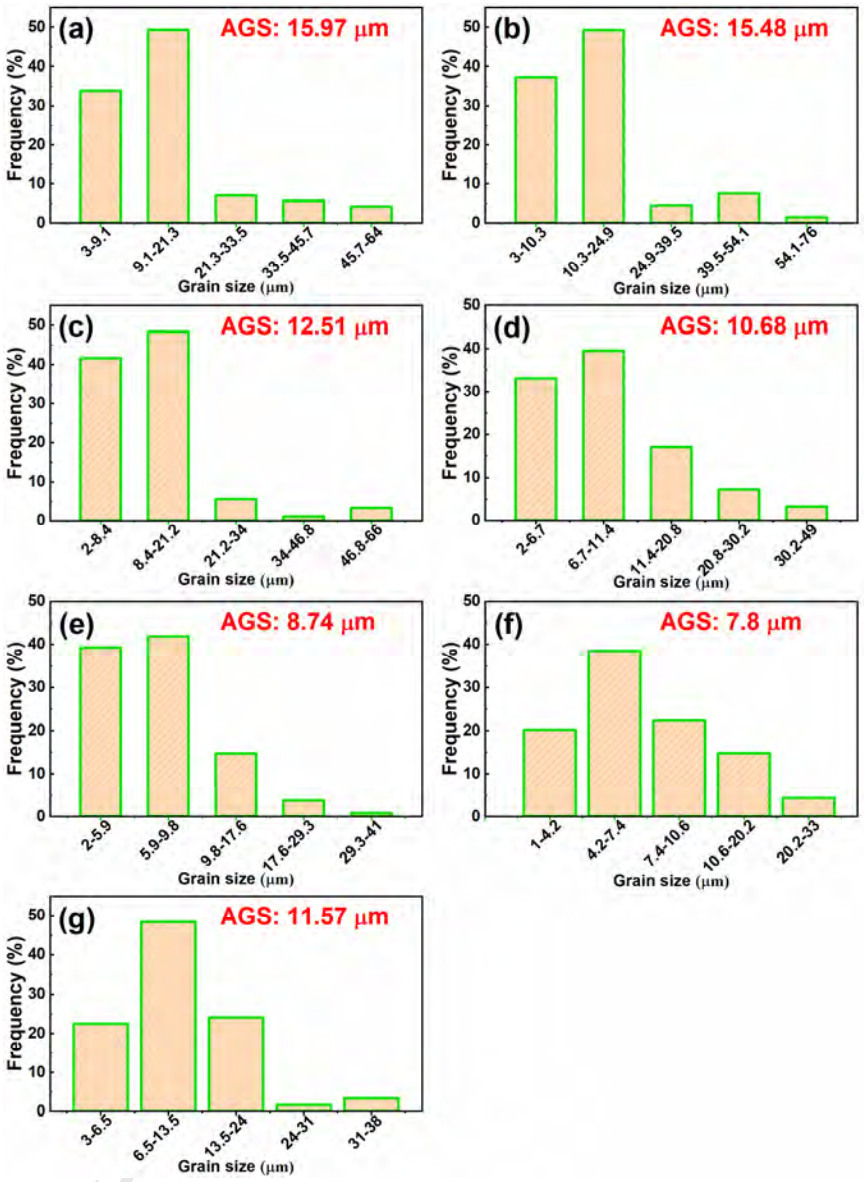

Figure 4. The distributions of grain size for $Ca_{0.61}Nd_{0.26}Ti_{1-x}Cr_xO_3$ ($0 \leq x \leq 0.03$) ceramics sintered at 1400 ºC with (a) x = 0; (b) x = 0.005; (c) x =0.01; (d) x = 0.015; (e) x = 0.02; (f) x = 0.025; (g) x = 0.03. The AGS indicates the average grain size.

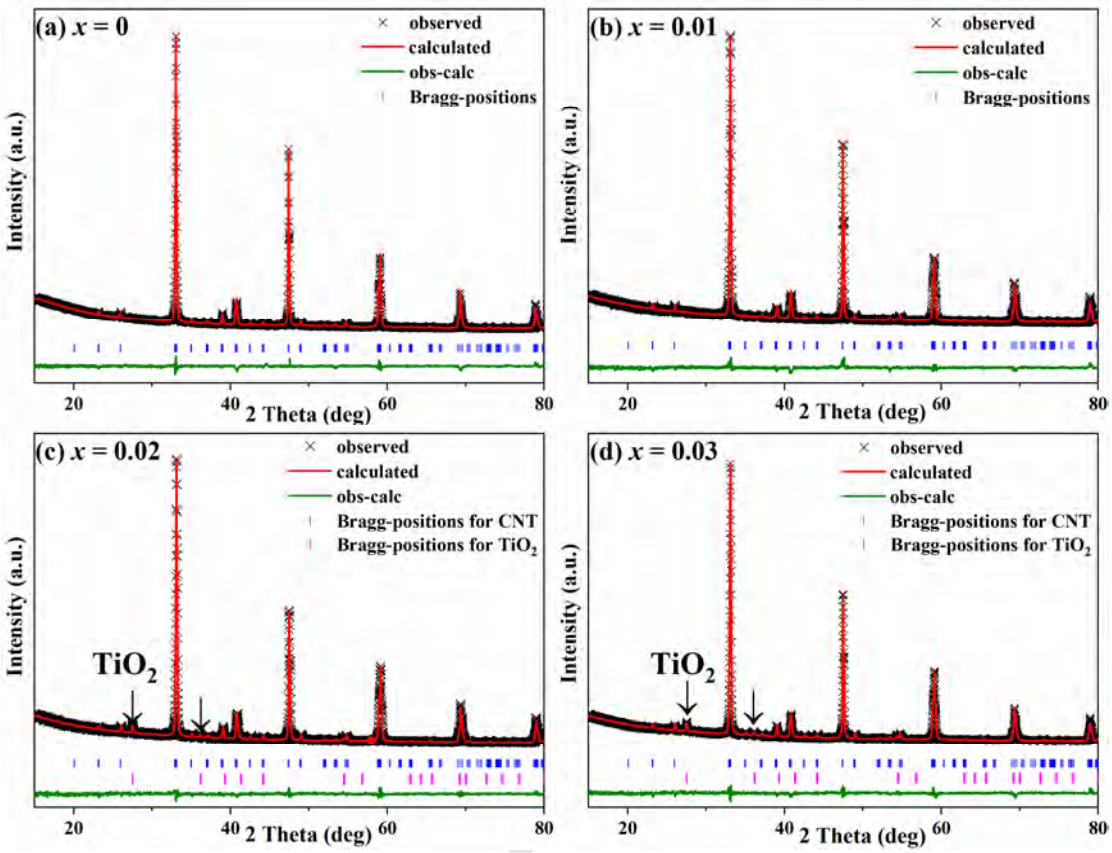

Figure 5. XRD profile of $Ca_{0.61}Nd_{0.26}Ti_{1-x}Cr_xO_3$ ($0 \leq x \leq 0.03$) ceramics sintered at 1400 ºC based on the Rietveld refinement with (a) x = 0; (b) x = 0.01; (c) x =0.02; (d) x = 0.03 (CNT refers to $Ca_{0.61}Nd_{0.26}TiO_3$).

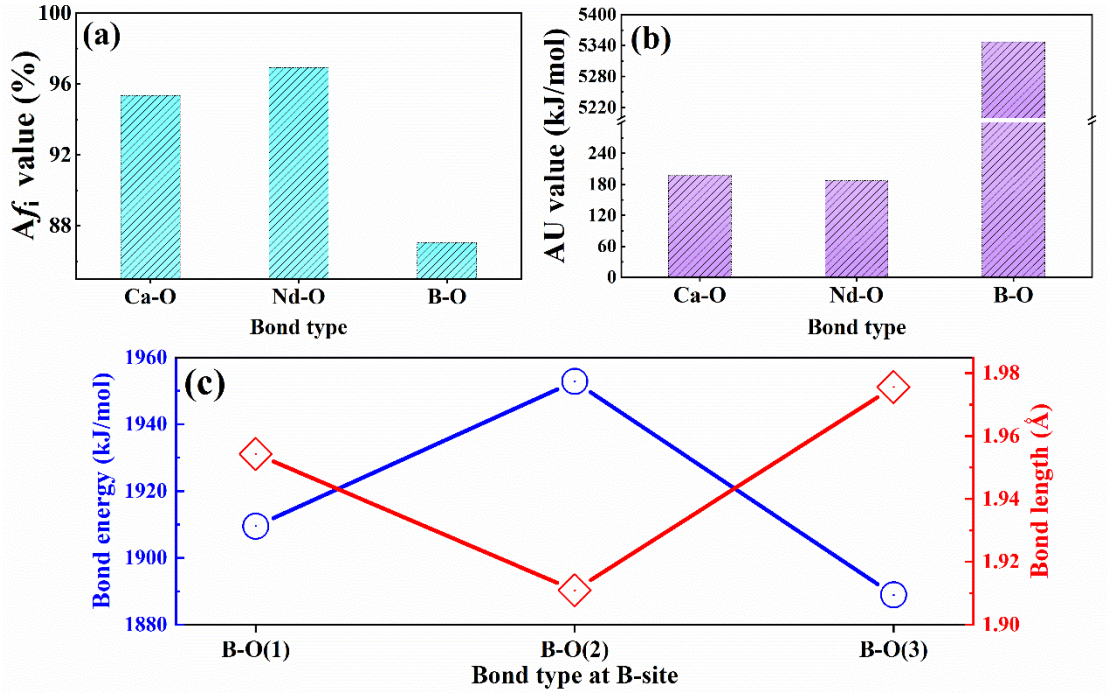

Figure 6. Bond characteristics for $Ca_{0.61}Nd_{0.26}TiO_3$ ceramic (x = 0) with (a) average bond ionicity

of different bonds; (b) average lattice energy of different bonds; (c) bond energy and bond length of different bonds at B-site.

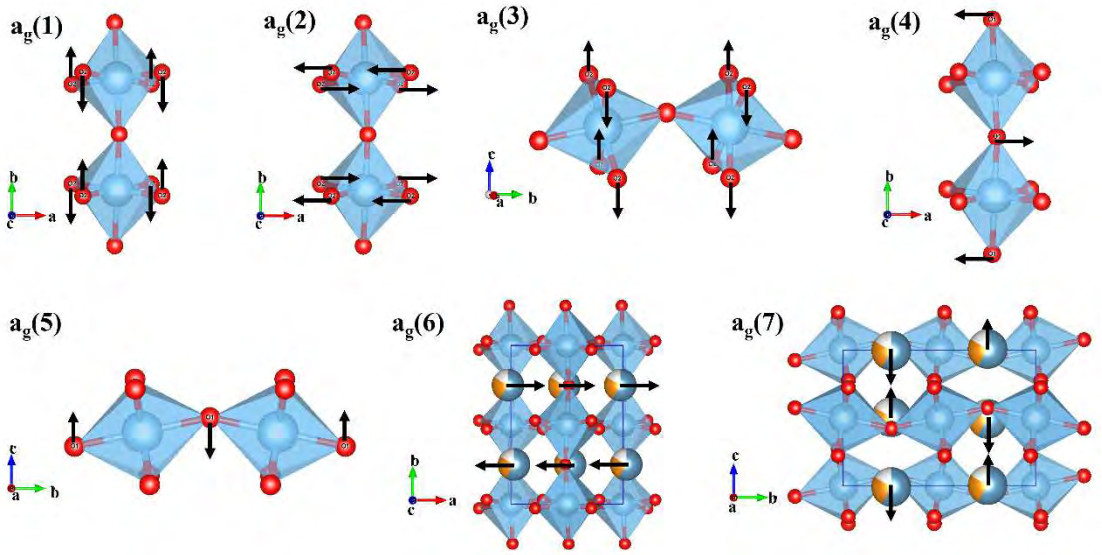

Figure 7. Schematic diagrams of the vibration symmetry coordinate a_g of the $Ca_{0.61}Nd_{0.26}TiO_3$ ceramic.

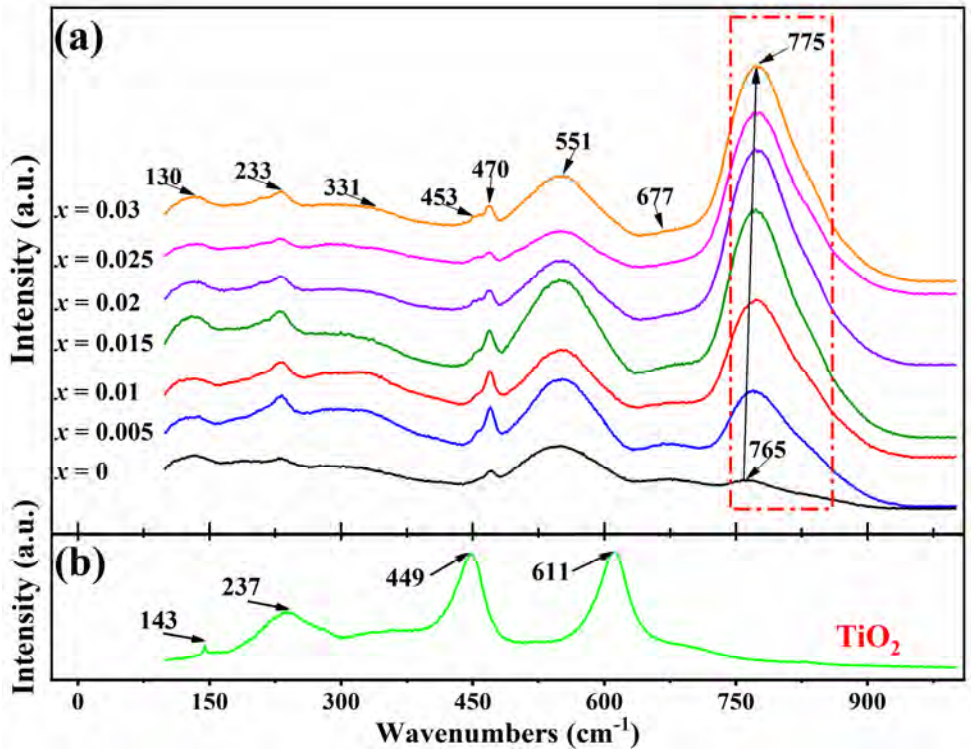

Figure 8. (a) Raman spectra of $Ca_{0.61}Nd_{0.26}Ti_{1-x}Cr_xO_3$ ($0 \leq x \leq 0.03$) ceramics sintered at 1400 ºC; (b) Raman spectrum of TiO_2.

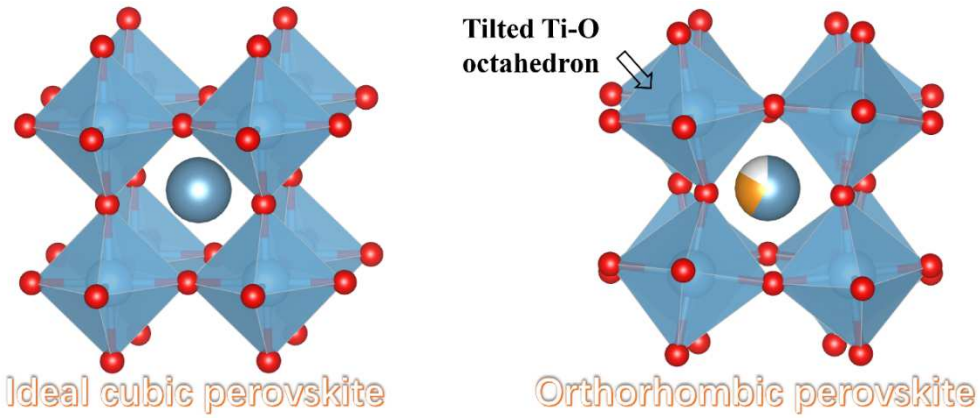

Figure 9. The contrast of ideal cubic perovskite with orthorhombic perovskite.

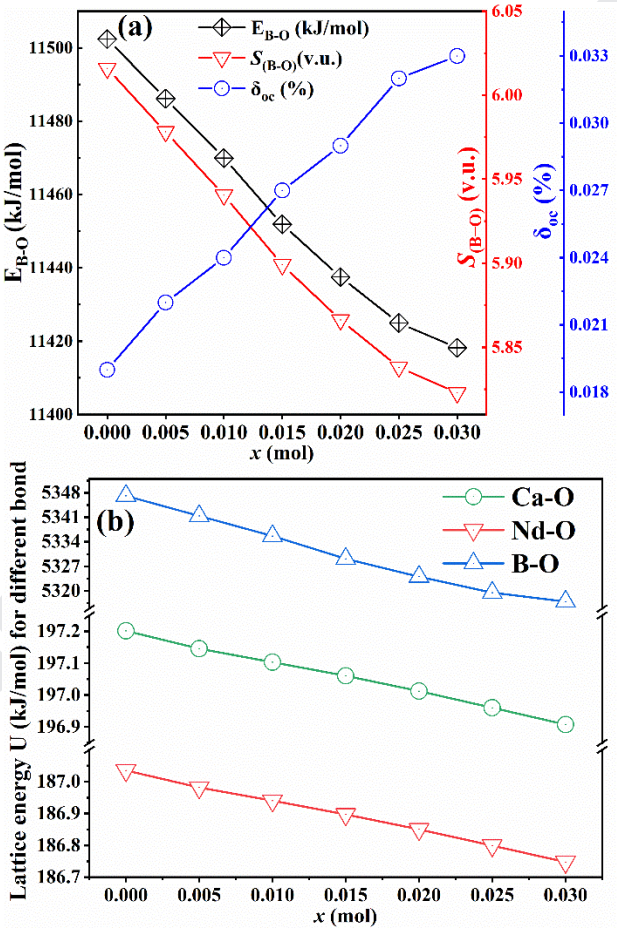

Figure 10. (a) Calculated B-site bond energies $E_{B\text{-}O}$ (kJ/mol), B-site bond strength ($S_{(B-O)}$) and oxygen octahedron distortion (δ_{oct}) for $Ca_{0.61}Nd_{0.26}Ti_{1-x}Cr_xO_3$ ($0 \le x \le 0.03$) ceramics sintered at 1400 ºC; (b) Lattice energy U (kJ/mol) for different bond in $Ca_{0.61}Nd_{0.26}Ti_{1-x}Cr_xO_3$ ($0 \le x \le 0.03$) ceramics sintered at 1400 ºC.

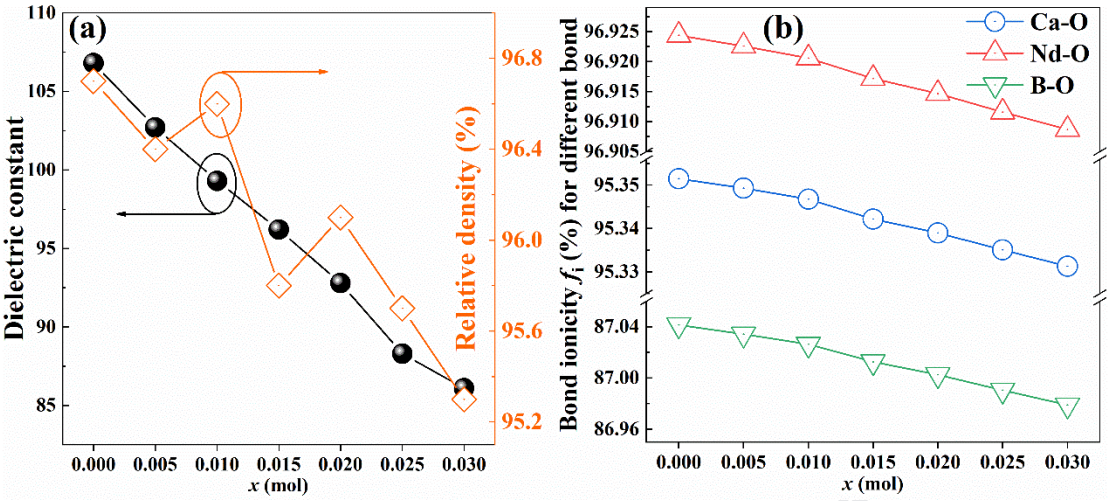

Figure 11. (a) Dielectric constant, relative density of $Ca_{0.61}Nd_{0.26}Ti_{1-x}Cr_xO_3$ ($0 \le x \le 0.03$) ceramics sintered at 1400 ºC; (b) Bond ionicity f_i for different bond in $Ca_{0.61}Nd_{0.26}Ti_{1-x}Cr_xO_3$ ($0 \le x \le 0.03$) ceramics sintered at 1400 ºC.

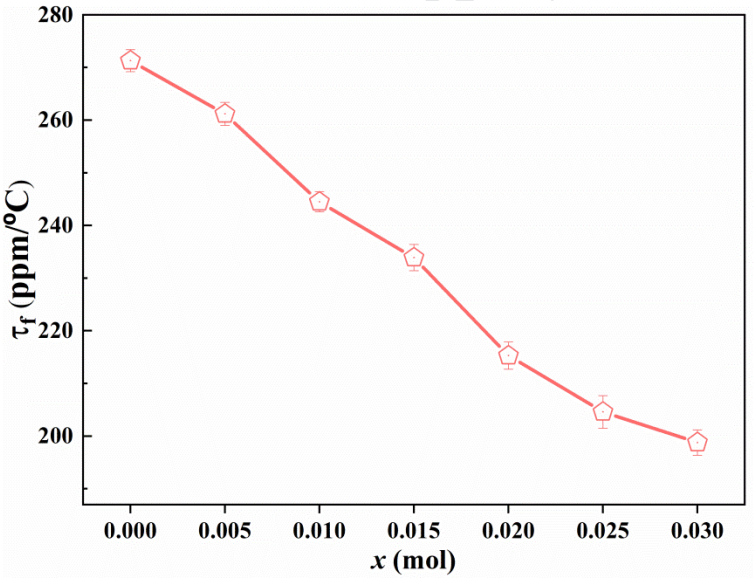

Figure 12. τ_f values of $Ca_{0.61}Nd_{0.26}Ti_{1-x}Cr_xO_3$ ($0 \le x \le 0.03$) ceramics sintered at 1400 ºC.

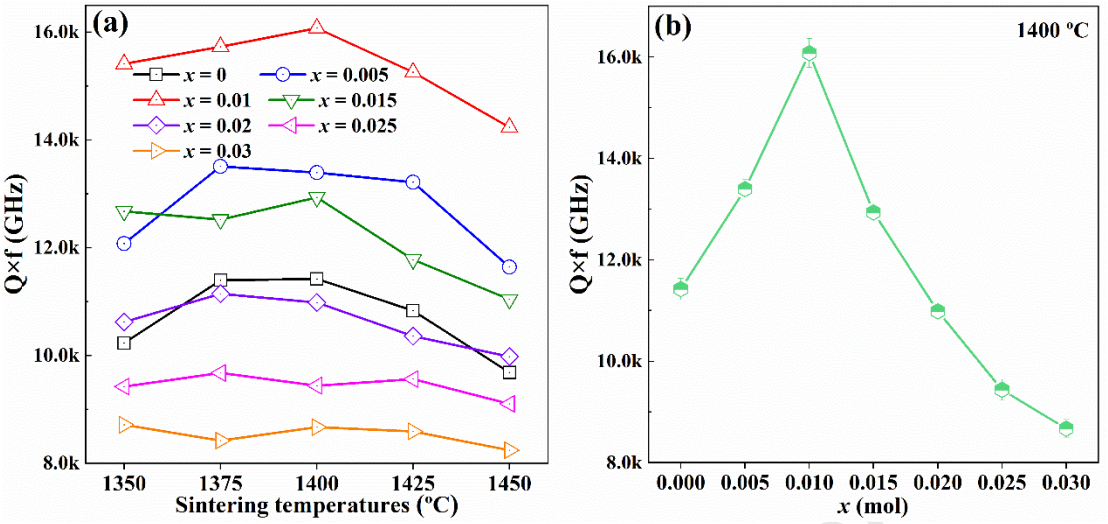

Figure 13. Q×f values of $Ca_{0.61}Nd_{0.26}Ti_{1-x}Cr_xO_3$ ($0 \leq x \leq 0.03$) ceramics. (a) samples sintered at different temperatures; (b) variation of Q×f value for samples sintered at1400 °C as a function of *x* value.

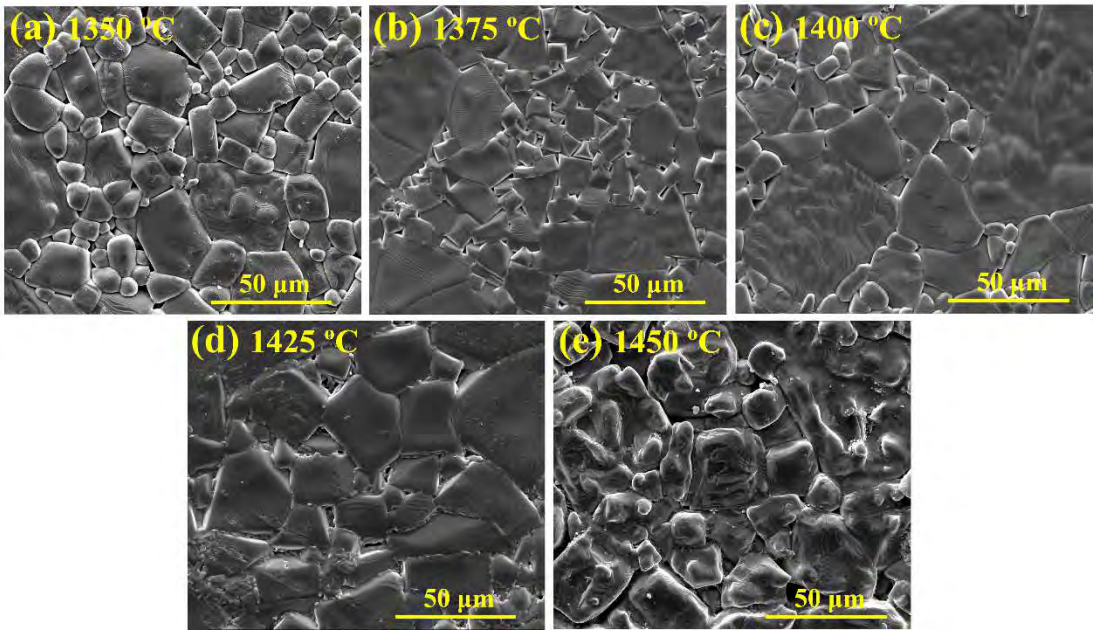

Figure 14. SEM images of $Ca_{0.61}Nd_{0.26}Ti_{1-x}Cr_xO_3$ (x = 0.01) ceramics sintered at different temperatures.

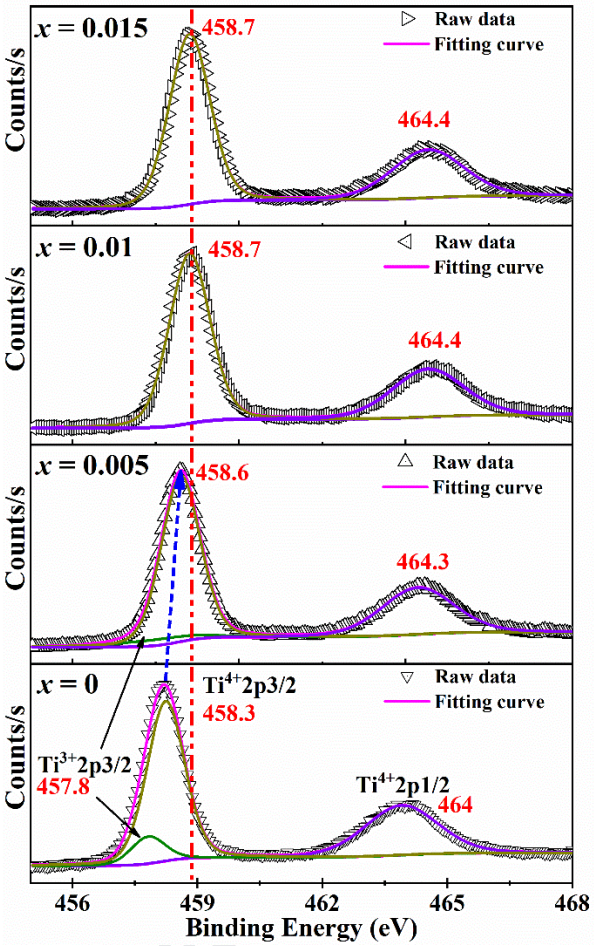

Figure 15. Ti-2p Core level XPS and corresponding fitting results for $Ca_{0.61}Nd_{0.26}Ti_{1-x}Cr_xO_3$ ($0 \leq x \leq 0.015$) ceramics sintered at 1400 ºC.

1. The $Ca_{0.61}Nd_{0.26}Ti_{0.99}Cr_{0.11}O_3$ ceramic had maximum Q×f value of 16,078 GHz.
2. The SRO effect enhanced with increase of Cr^{3+}.
3. The balanced amount of Cr substitution could restrain the generation of Ti^{3+}.

Declaration of interests

☒ The authors declare that they have no known competing financial interests or personal relationships that could have appeared to influence the work reported in this paper.

☐The authors declare the following financial interests/personal relationships which may be considered as potential competing interests: